APPENDIX A: K2 PHOTOMETRIC DATA ANALYSIS

We analysed the K2 data discussed in Section 2.2. From these data sets, the flux (in $e^- s^{-1}$), F_i, over a set of N sample times, t_i, with indices $i = \{0, 1, 2, ..., N-1\}$, was analysed to search for photometric variability. The analysis processes, as described below, were applied to the long cadence data of all stars. The analysis of the short cadence data acquired for HD 73045 was performed in a similar manner.

To begin, each time step, t_i, was defined in a way that $t_0 = 0$; this was done by subtracting the original Barycentric Julian Date (BJD) times, τ_i, by that of the first point, τ_0, using

$$t_i = \tau_i - \tau_0, \tag{A1}$$

where τ_0 = 2 457 139.63 days, 2 458 095.49 days, and 2 458 251.57 days for C05, C16, and C18, respectively.

The flux data were re-calibrated as a magnitude deviation, Δm_i, of each flux, F_i, from its mean, $\langle F \rangle$. For all N data points in a data set, at a corresponding time, t_i, the i-th magnitude deviation data point in the series is defined by

$$\Delta m_i = -2500 \log_{10} \left(\frac{F_i}{\langle F \rangle} \right), \tag{A2}$$

where Δm_i is calculated in mmag (hence the incorporated factor of 1000). To prepare these data for the signal analysis process, variable artifacts, such as those possibly left over from the PDC process were removed by subtracting an eighth order polynomial, although it is noted that such artifact removal may also cancel any intrinsic variability component of a corresponding frequency. Subsequently, the signal search was focused on periods shorter than 20 days. The median value of the data was also subtracted. As an example, the analysed photometric light curve of HD 73045 obtained during C18 campaign is shown in Fig. 3 (top-left, blue points).

To analyse a light curve in the frequency domain, the Lomb-Scargle (LS) algorithm (Lomb 1976; Scargle 1989) was applied to the time-series data, noting that the original SAP data are irregularly sampled. The Nyquist frequency $(2dt)^{-1}$ for LC (29.4 min cadence) and SC (58.8 s cadence) sampling are ~24.5 d^{-1} and ~735 d^{-1}, respectively. Each campaign occupies its own temporal range T, giving in a respective frequency resolution, Δf. For example, C18 has a temporal window of T = 50.814 d, providing a frequency resolution of $\Delta f = 0.0197\ d^{-1}$ that allows an estimate for the peak frequencies and corresponding amplitudes. To improve signal peak definition and to better estimate the peak frequencies and amplitudes, oversampling was applied to provide a frequency domain sampled every 0.001 d^{-1}. Although the half-width at half-maximum (HWHM) of a peak is often used to estimate the accuracy of the peak frequency, VanderPlas (2018) suggests avoiding this approach through computing the false-alarm probability (FAP) for each peak. This criterion estimates the probability that a peak was produced by noise as opposed to an inherent signal. The lower the value of the FAP, the more likely that a given peak is real. Furthermore, Frescura et al. (2008) noted the subjectivity of the noise level determination in calculating the signal-to-noise ratio, which is often used to select relevant peaks from the background noise spectrum (Breger et al. 1993). Therefore, while the amplitude signal-to-noise value was calculated for candidate signal peaks, through the use of a smoothing function across the frequency spectrum to calculate the noise spectrum, the FAP was used as the selection criterion to determine a signal's validity. For this study, the independent frequency method (VanderPlas 2018) was applied to calculate the FAPs of respective spectral amplitudes across the frequency domain. After a provisional analysis, a threshold FAP of 10^{-8} was adopted across all data sets to provide a consistent, conservative criterion for identifying true signals amongst the noise, which is noted by Bowman et al. (2018) to be particularly significant at low frequencies. An example periodogram (logarithm of the period versus amplitude) is shown in Fig. 3 (bottom, blue-line) for the C18 data set for HD 73045. The frequencies, periods, and amplitudes for peaks with FAP values of 10^{-8} and below, for all stars during their respective campaigns as a result of performing the Lomb-Scargle analysis are listed in Table A1.

Next, the time-series data were analysed to determine the frequency, f, amplitude, A, and the phase at $t_0 = 0$, $\phi(t_0)$, from which a model of the light curve was constructed. Using the results of the Lomb-Scargle analysis as initial starting points, sinusoidal components incorporating these parameters were determined by sequentially fitting a series of components in the form of a sinusoid plus an offset, Z, to the data:

$$\Delta m_i = Z + A \sin(2\pi f t_i + \phi), \tag{A3}$$

where ϕ is the phase derived from the fit and is described below.

Using the methods of Montgomery & O'Donoghue (1999), the corresponding errors, $\sigma(f)$, $\sigma(A)$, and $\sigma(\phi)$, were also derived using:

$$\sigma(f) = \sqrt{\frac{6}{\mathcal{N}}} \frac{1}{\pi \mathcal{T}} \frac{\sigma(\Delta m)}{A}, \tag{A4}$$

$$\sigma(A) = \sqrt{\frac{2}{\mathcal{N}}} \sigma(\Delta m), \tag{A5}$$

$$\sigma(\phi) = \sqrt{\frac{2}{\mathcal{N}}} \frac{\sigma(\Delta m)}{A}. \tag{A6}$$

Here, $\mathcal{N}$ is the number of terms in a regularly sampled time series with an interval Δt, $\mathcal{T} = \mathcal{N}\Delta t$ is the time range of the data set, A is the amplitude of the sinusoidal fit, and $\sigma(\Delta m)$ is the root mean square of the flux deviation values.

To determine these sinusoidal parameters and their uncertainties, the data were resampled at the regular 29.4-min cadence using cubic spline interpolation. Next, the time was adjusted such that the zero point was placed at the center of the data set by subtracting the average of the resampled time array. Using the Lomb-Scargle results as a starting point, single sinusoids were sequentially fit using Eqn. A3 and subtracted from the time-series, until all components (i.e., those with Lomb-Scargle FAP values below the threshold) were accounted for. The fitting process allowed the amplitude to vary within 20 per cent about its LS value, while the frequency was allowed to vary within 0.01 d^{-1} about its input value. From the resulting phase value, ϕ, which is determined at this central point, the phase of the first point of the fit, $\phi(t_0)$, was calculated.

For any component with a variation period P, the phase of each data point ϕ_i, at time t_i relative to the first point in the data series at time t_0, can be calculated using

$$\phi_i = 2\pi \left(\frac{t_i - t_0}{P} - \left\lfloor \frac{t_i - t_0}{P} \right\rfloor \right), \tag{A7}$$

which simplifies when $t_0 = 0$. From this, phase-folded plots of the time-series were produced corresponding to the dominant period of each star for each campaign. The C18 HD 73045 data are folded to the dominant period of 12.64 d in Fig. 3 (top-right) along with a sinusoidal fit to this component (red-line) with the parameters given in Table 3.

Table A1. Flux variation signal properties (ordered by amplitude) derived from applying the Lomb-Scargle analysis to the all flux-deviation data sets. For HD 73045, C18, refer to the blue-line peaks of Fig. 3 (bottom).

Star Name	Campaign	Frequency (d^{-1})	Period (d)	Amplitude (mmag)	$\log_{10}$(FAP)
HD 73045	C05	0.078	12.82	0.112	-302
		0.155	6.452	0.039	-33
		0.054	18.52	0.0309	-18
		0.138	7.246	0.029	-17
		0.171	5.848	0.022	-8
	C18	0.079	12.66	0.039	-95
		0.155	6.452	0.022	-29
HD 76310	C05	0.217	4.608	0.498	-361
		0.186	5.376	0.189	-49
		0.421	2.375	0.113	-15
		0.049	20.41	0.105	-13
		0.159	6.289	0.095	-10
	C16	0.209	4.785	0.398	-331
		0.187	5.348	0.333	-231
		0.076	13.16	0.104	-19
		0.430	2.326	0.089	-13
		0.969	1.031	0.081	-11
		0.058	17.24	0.072	-8
	C18	0.206	4.854	1.094	-420
		0.177	5.650	0.275	-24
		0.430	2.326	0.188	-9
HD 73574	C05	0.070	14.29	0.8139	-76
		0.091	10.99	0.3827	-14
	C18	0.091	10.99	0.0513	-9
HD 73618	C05	0.264	3.788	0.415	-274
		0.205	4.878	0.228	-81
		0.410	2.439	0.152	-34
		0.244	4.098	0.104	-14
		0.431	2.320	0.102	-13
		0.184	5.435	0.086	-9
	C16	0.261	3.831	0.320	-254
		0.205	4.878	0.287	-203
		0.401	2.494	0.137	-44
		0.225	4.444	0.135	-43
		0.418	2.392	0.104	-24
		0.242	4.132	0.094	-19
		0.290	3.448	0.074	-10
		0.448	2.232	0.069	-9
	C18	0.266	3.759	0.595	-256
		0.213	4.695	0.249	-42
		0.196	5.102	0.194	-24
		0.417	2.398	0.190	-23
		0.238	4.202	0.125	-8
		0.295	3.390	0.123	-8
HD 73619	C05	0.077	12.987	0.388	-289
		0.155	6.452	0.210	-82
		0.233	4.292	0.160	-46
		0.058	17.241	0.108	-19
		0.042	20.810	0.098	-16
		0.310	3.226	0.095	-14
		0.096	10.417	0.082	-10
	C18	0.077	12.987	0.324	-217
		0.156	6.410	0.163	-52
		0.235	4.256	0.103	-19
		0.112	8.929	0.075	-9

APPENDIX B: SUPPLEMENTARY MATERIALS

Table B1. Ground-based CCD photometric observations of HD 73045 obtained from various optical telescopes located at different sites.

S. No.	Observatory	Telescope Diameter (m)	Filters	Exposure Time (s)	Total Durations (h)	Date dd-mm-yyyy	HJD (d)
1.	ARIES	1.04	V	2	1.47	16-04-2014	2456764
2.			V	3	0.92	20-04-2014	2456768
3.			B	5	2.53	21-04-2014	2456769
4.	Devasthal	1.30	B	5	1.80	02-11-2014	2456964
5.			V	4	1.47	11-11-2014	2456973
6.			B	4	0.17	30-11-2014	2456992
7.			V	15	0.85	30-12-2015	2457387
8.			V	10	0.57	27-01-2016	2457415
9.			B	15	2.12	28-01-2016	2457416
10.			V	3	2.02	19-12-2016	2457742
11.	MASTER-II	0.40	B, V	5	2.92, 2.92	09-11-2015	2457336
12.	-URAL		B	5	1.35	22-01-2016	2457410
13.			B, V	5	0.13,0.13	13-02-2016	2457432*
14.			B	5	4.00	11-03-2016	2457459
15.			V	5	3.97	14-03-2016	2457463
16.			B, V	5	3.96, 3.96	15-03-2016	2457478
17.	PROMPT-8	0.60	B	4	1.26	12-05-2014	2456790
18.			B	4	0.27	14-05-2014	2456792
19.			B	4	1.65	16-05-2014	2456794
20.			B	15	1.10	11-01-2015	2457033
21.			B	20	1.21	09-02-2015	2457062

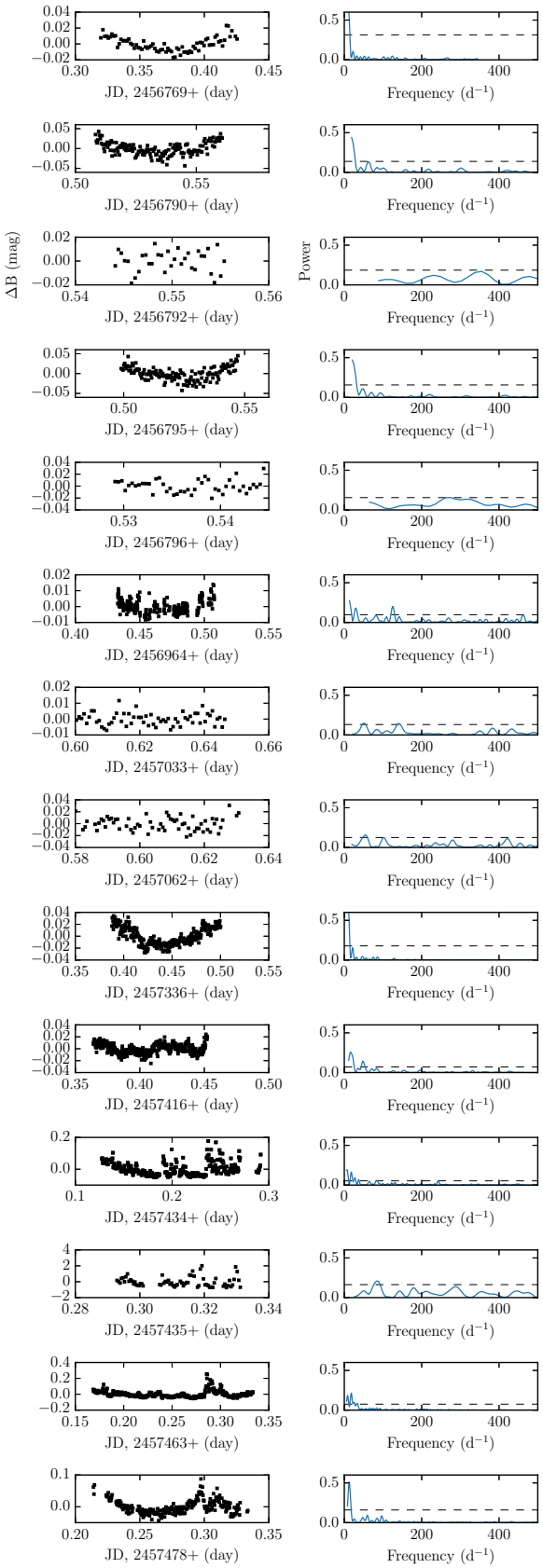

Figure B1. Light curves for HD 73045 from ground-based observations with B-filter.

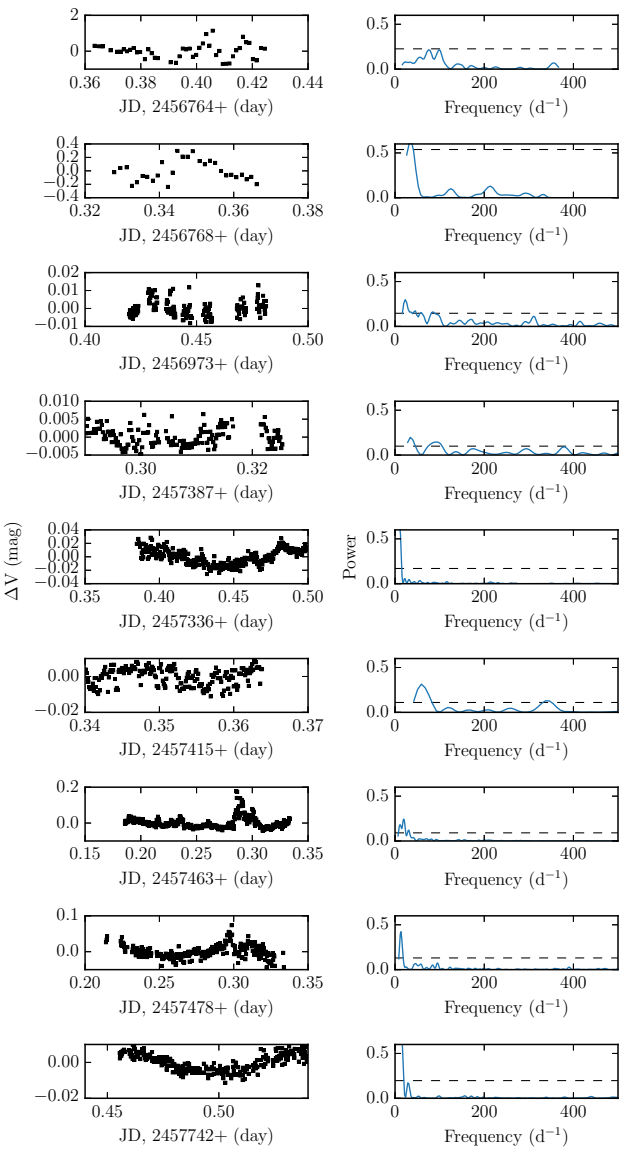

Figure B2. Light curves for HD 73045 from ground-observations with V-filter.

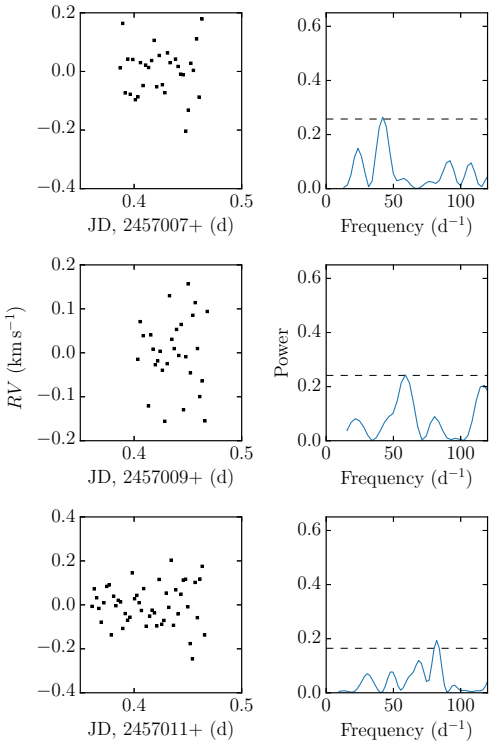

Figure B3. RV curve (*panels on the left*) and power spectrum (*panels on the right*) of the radial velocity measurements for HD 73045 from MRES data. The black horizontal dashed line in the power spectrum represents SNR of 4.

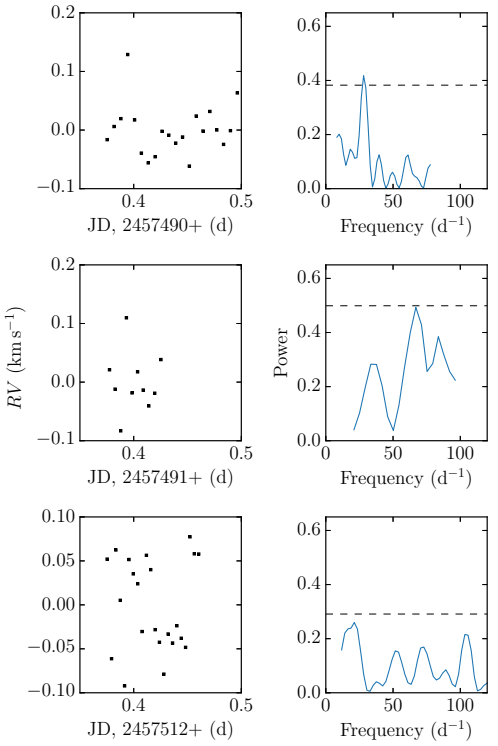

Figure B4. RV curve (*panels on the left*) and power spectrum (*panels on the right*) of the radial velocity measurements for HD 73045 from HERMES data. The black horizontal dashed line in the power spectrum represents SNR of 4.

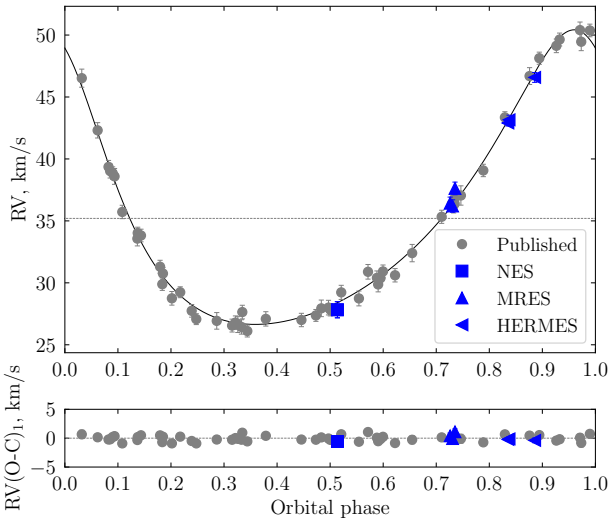

Figure B5. RV of HD 73045, as measured by us (blue), compared to the orbital solution by Carquillat & Prieur (2007) (grey).

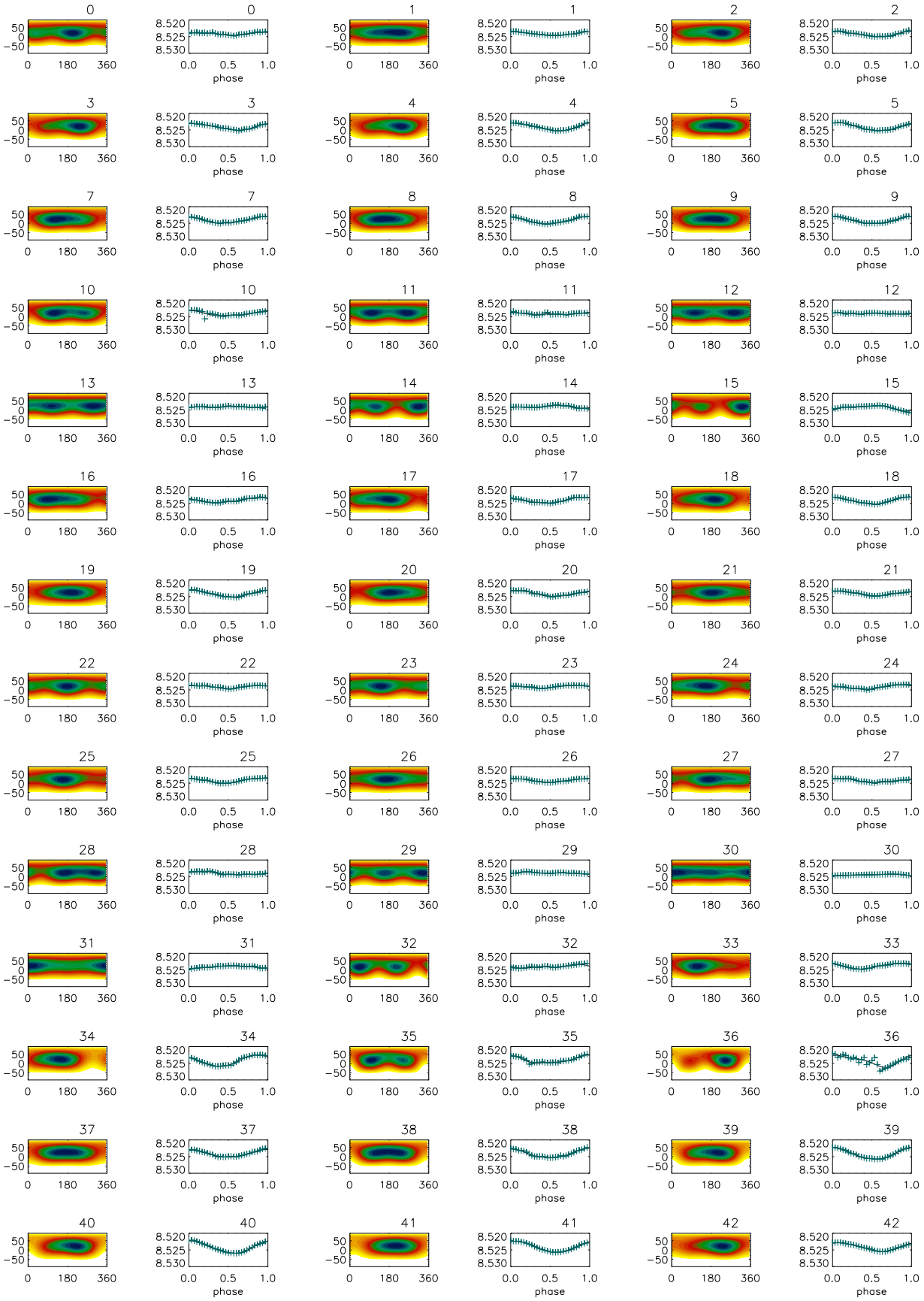

Figure B6. As Fig. 9, but spot maps for HD 76310.

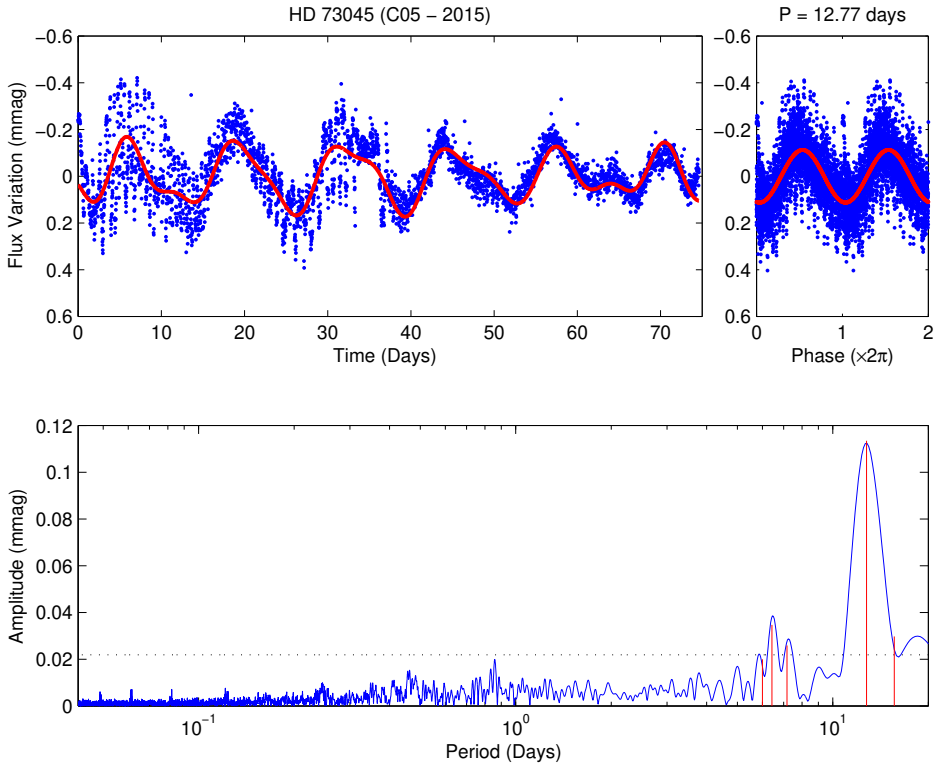

Figure B7. As Fig. 3, but for the LC *K2* Campaign 5 observations of HD 73045.

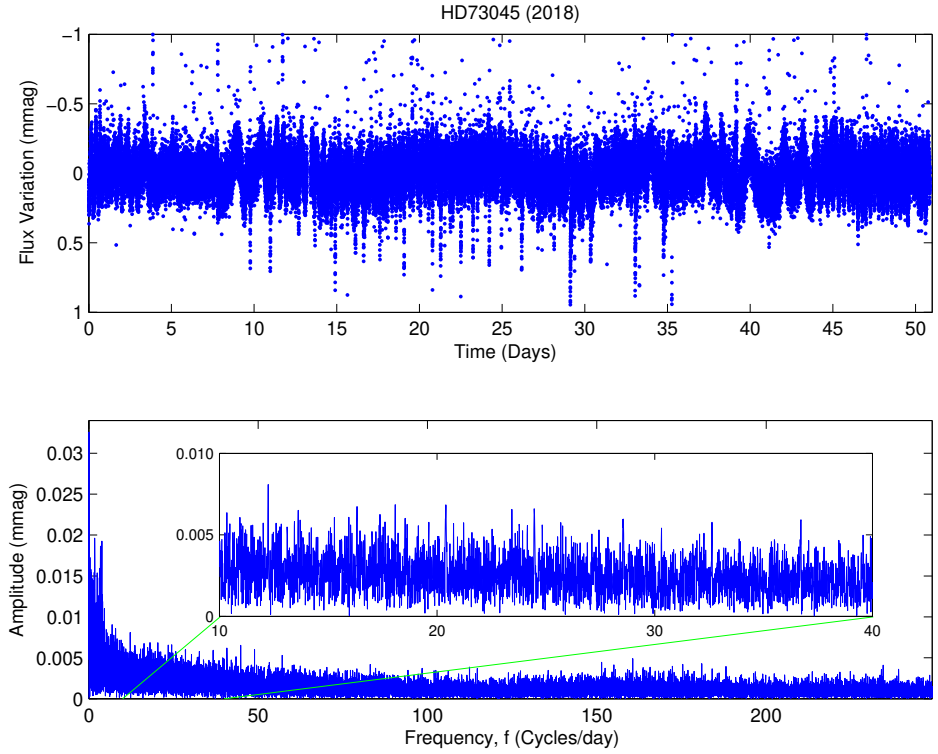

Figure B8. Top: Time series photometric variability (in mmag) of HD 73045 from the SC 2018 *K2* Campaign 18. The PDC_SAP data includes intrinsic signals as well as systemic and noise artifacts. Bottom: Frequency distribution of spectral amplitudes, in mmag, derived from applying the Lomb-Scargle algorithm to the time series. The frequency range from $10-40\,\mathrm{d}^{-1}$ is expanded into the inset to provide more detail of that range. It can be seen there are no signals related to those from the earlier ground-based observations and that this range is dominated by noise.

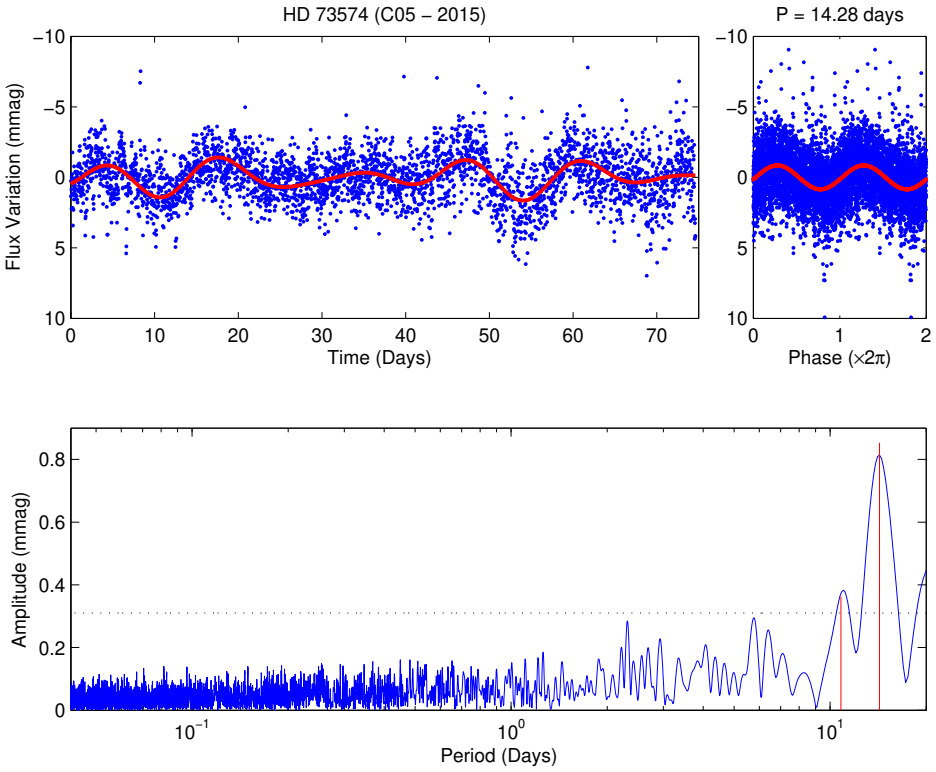

Figure B9. As Fig. 3, but for the LC *K2* Campaign 5 observations of HD 73574.

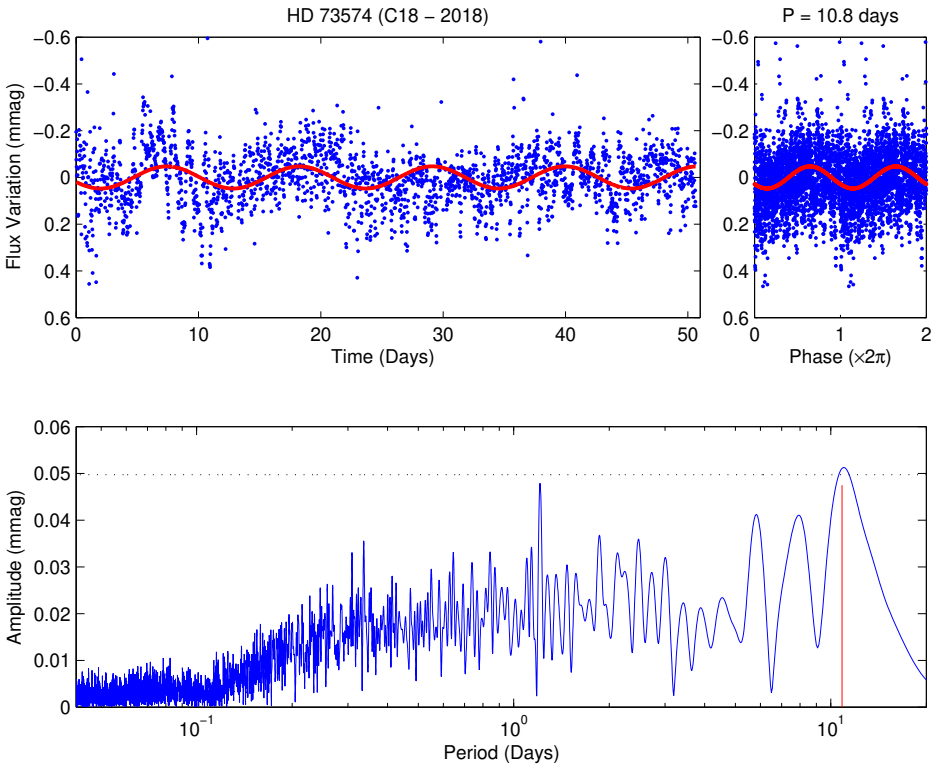

Figure B10. As Fig. 3, but for the LC *K2* Campaign 18 observations of HD 73574.

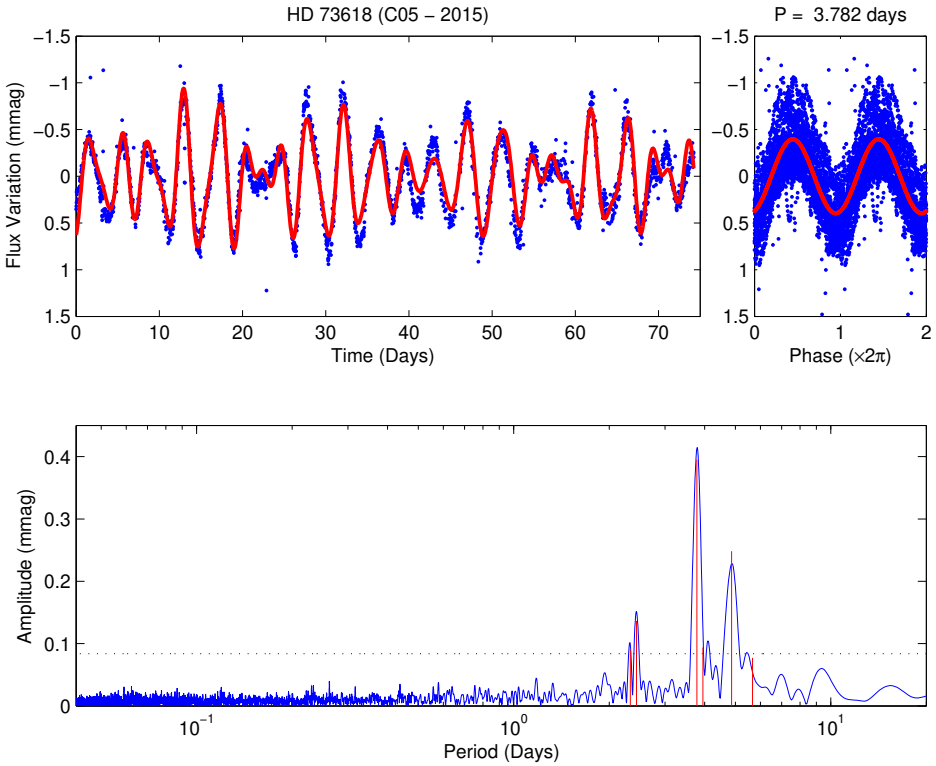

Figure B11. As Fig. 3, but for the LC *K2* Campaign 5 observations of HD 73618.

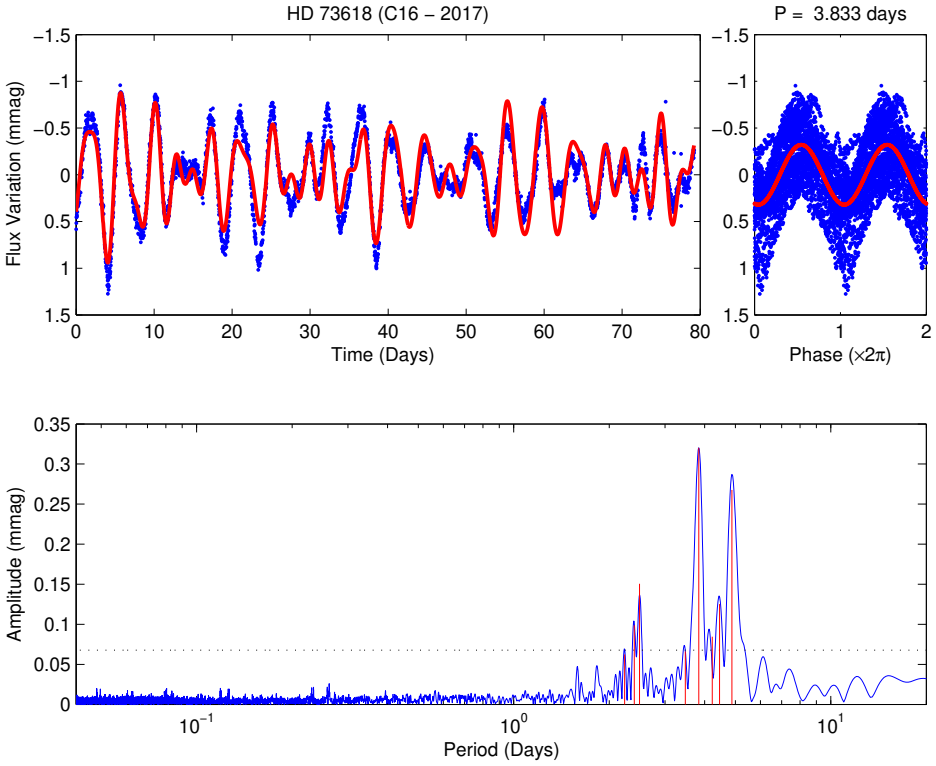

Figure B12. As Fig. 3, but for the LC *K2* Campaign 16 observations of HD 73618.

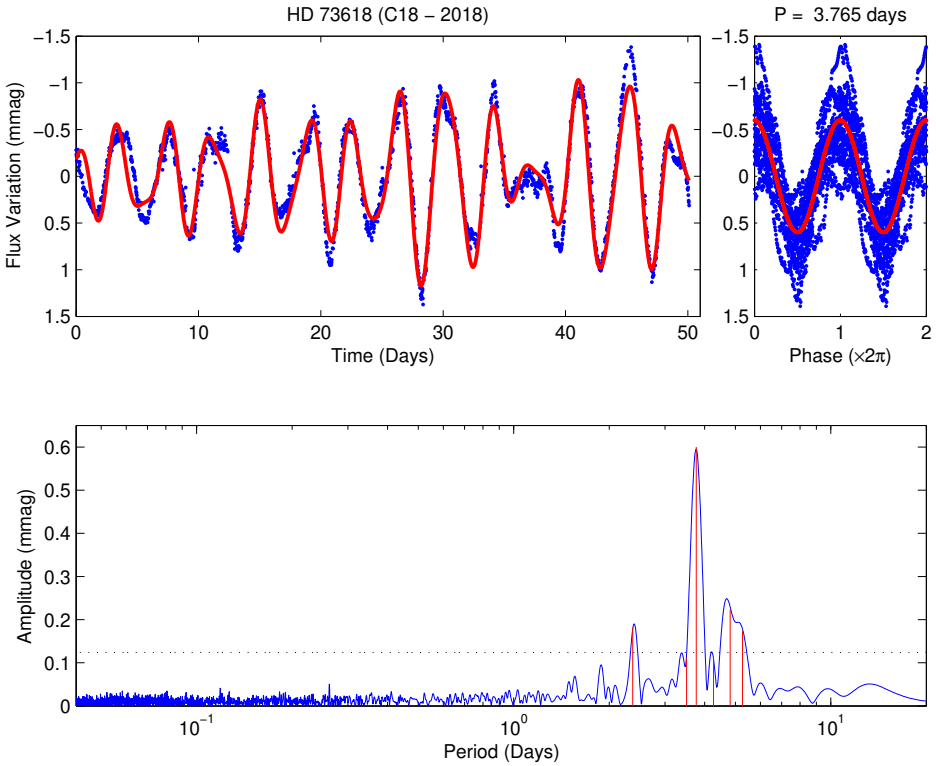

Figure B13. Time series (top) and respective Lomb-Scargle periodogram (bottom) for the LC *K2* Campaign 18 observations of HD 73618.

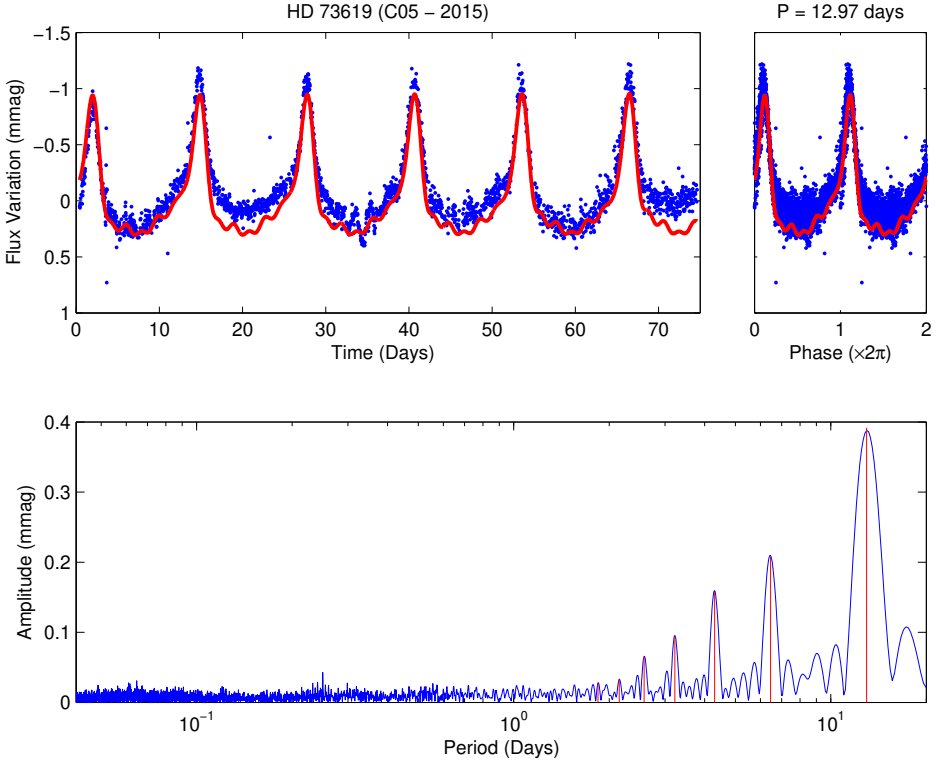

Figure B14. As Fig. 3, but for the LC *K2* Campaign 5 observations of HD 73619. However, in contrast to the remainder of this paper, the phase diagram is traced by two periods of the light curve model, and not by the dominant component. Additionally, the FAP threshold criterion has been removed, with the model being constructed from the fundamental component and its overtones.

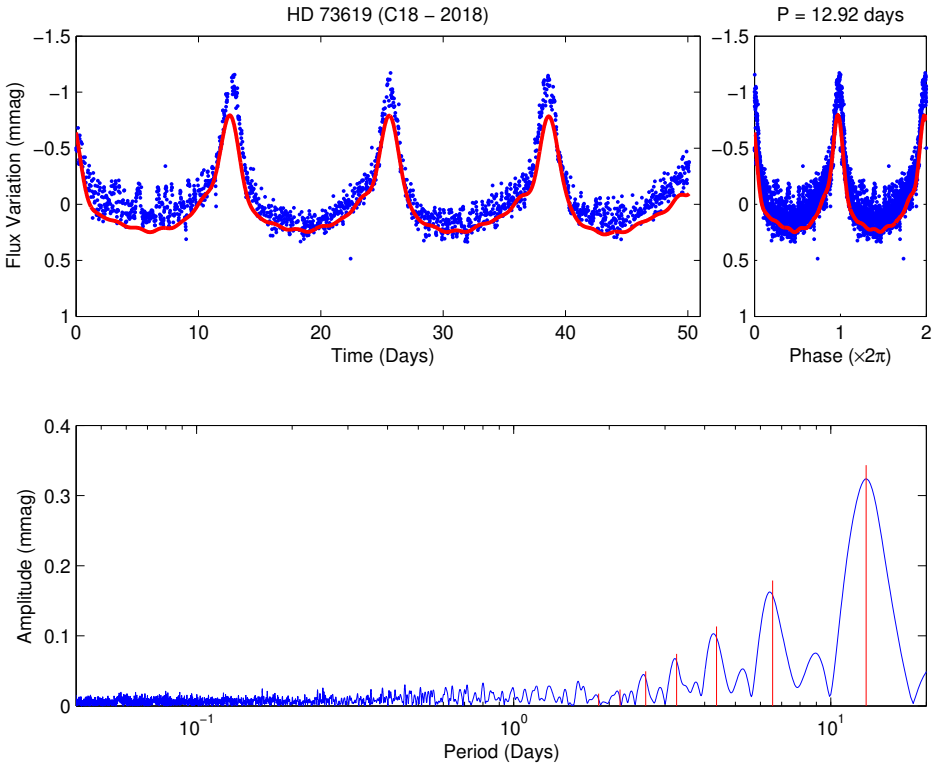

Figure B15. Time series (top) and respective Lomb-Scargle periodogram (bottom) for the LC *K2* Campaign 18 observations of HD 73619.

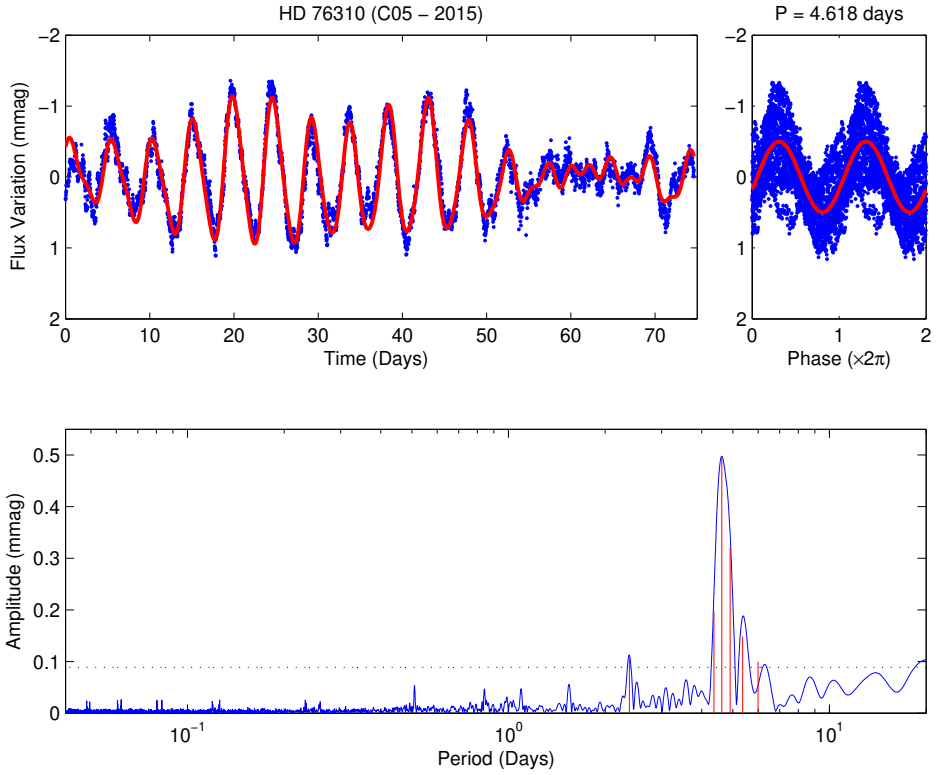

Figure B16. As Fig. 3, but for the LC *K2* Campaign 5 observations of HD 76310.

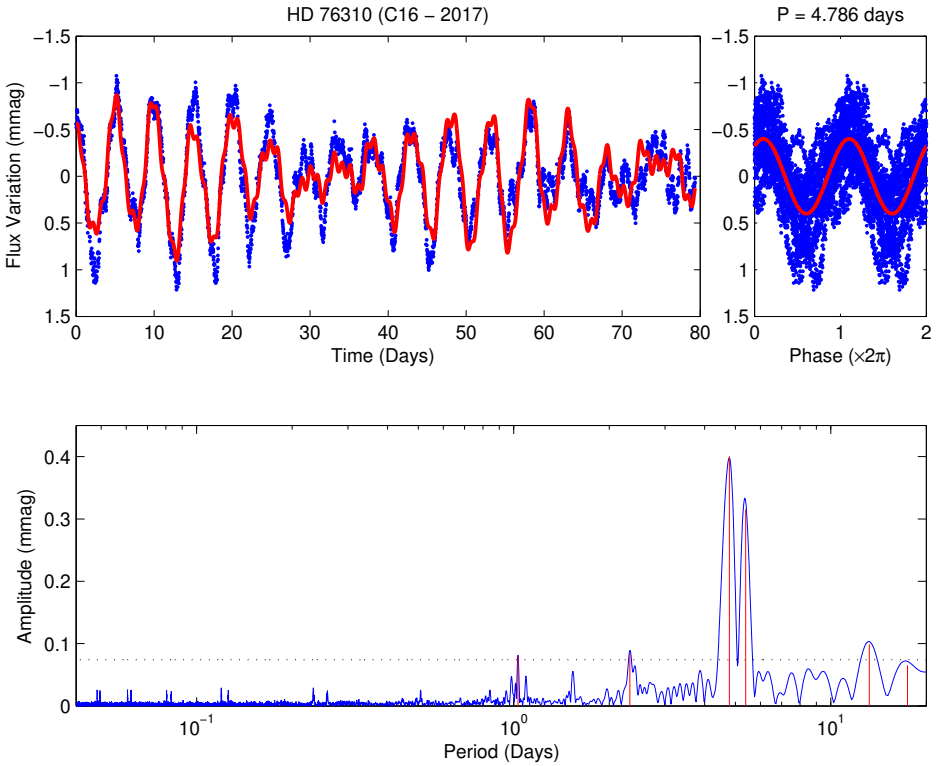

Figure B17. As Fig. 3, but for the LC *K2* Campaign 16 observations of HD 76310.

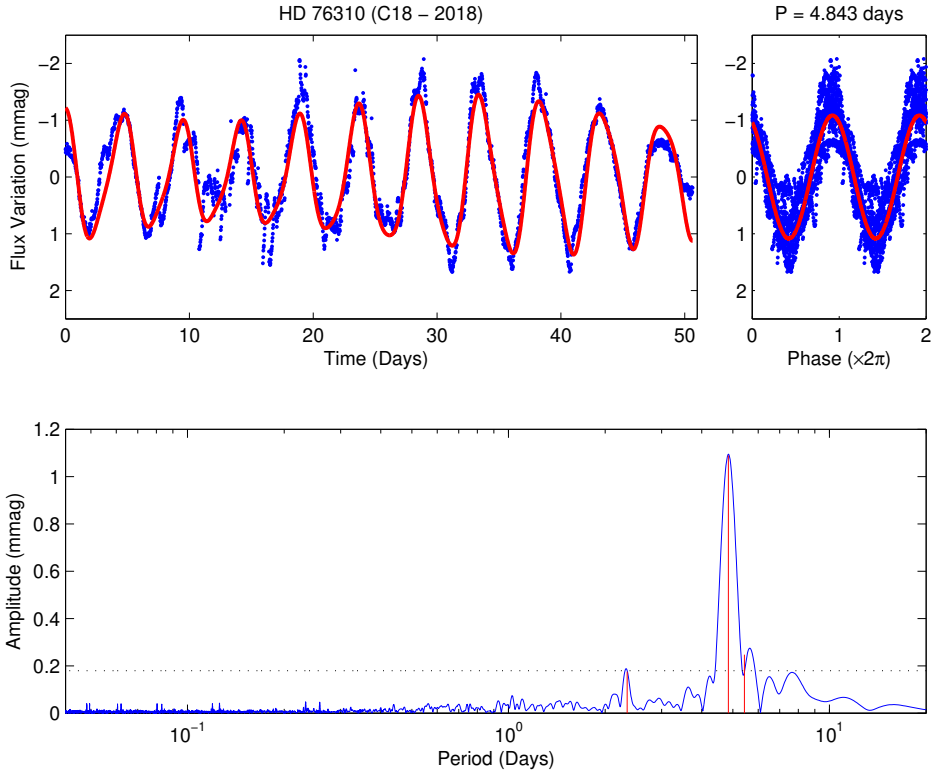

Figure B18. As Fig. 3, but for the LC *K2* Campaign 18 observations of HD 76310.

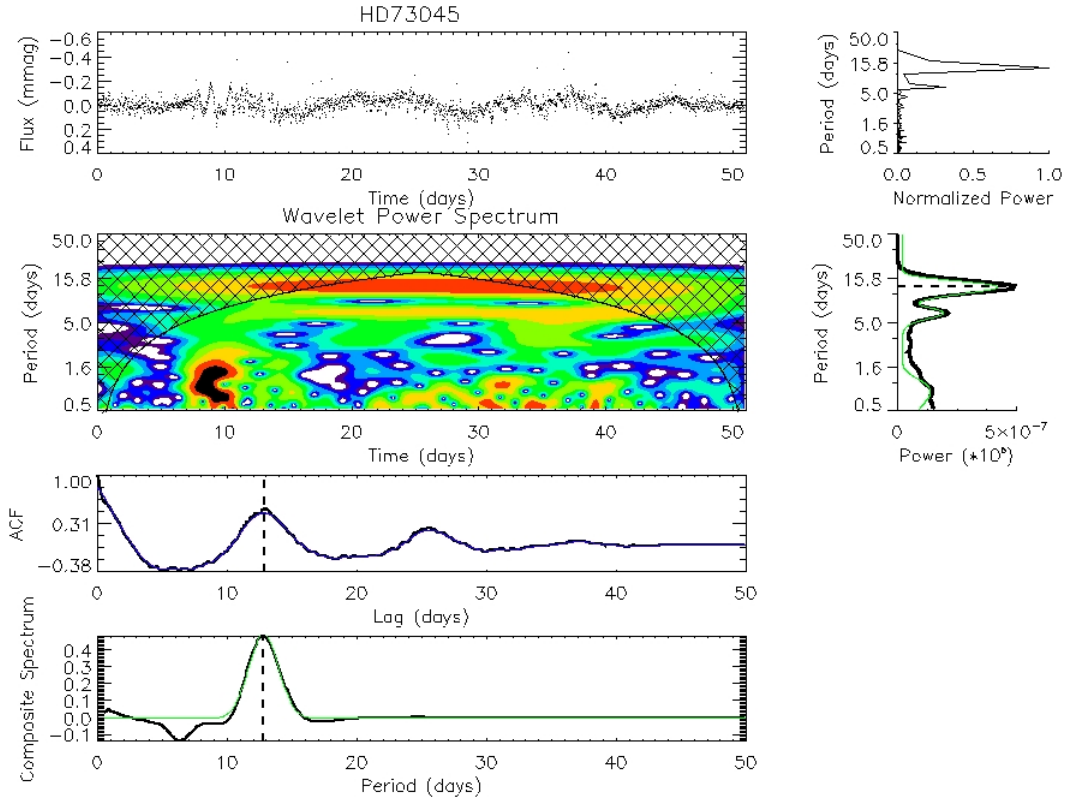

Figure B19. The wavelet map of HD 73045 based on *K2* C18 data; see Fig. 10 for description details.

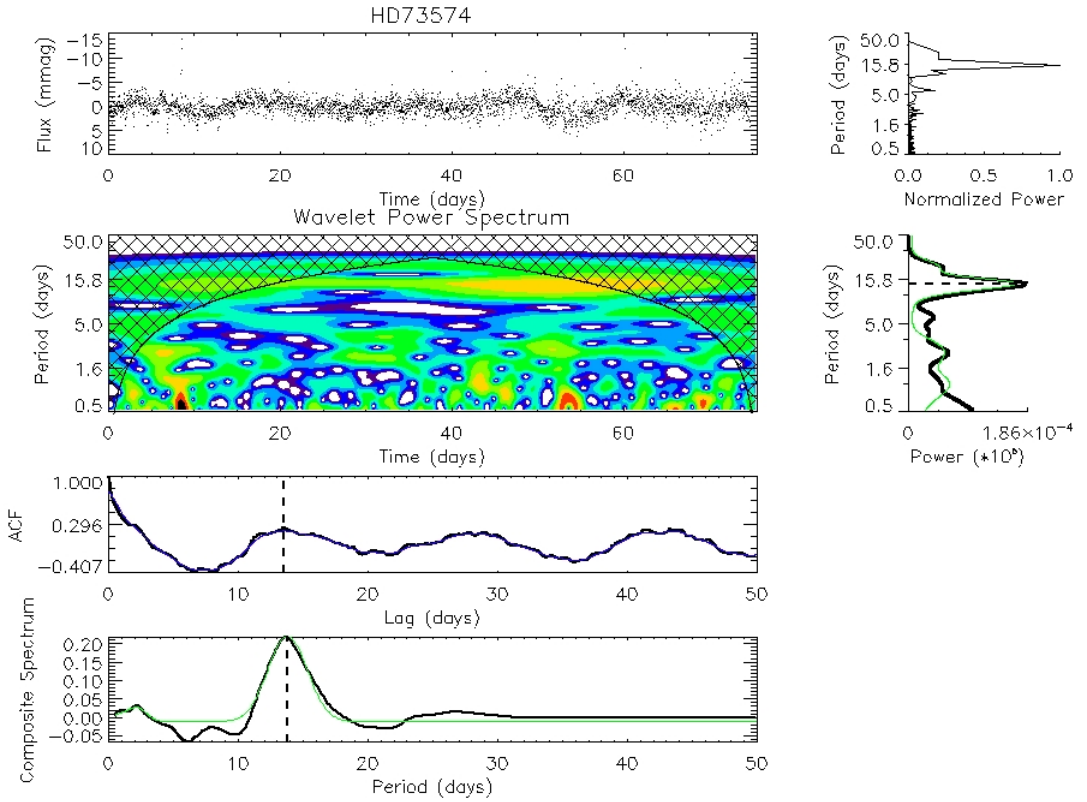

Figure B20. The wavelet map of HD 73574 based on C05 data. The description follows that for HD 73045, see Fig. 10.

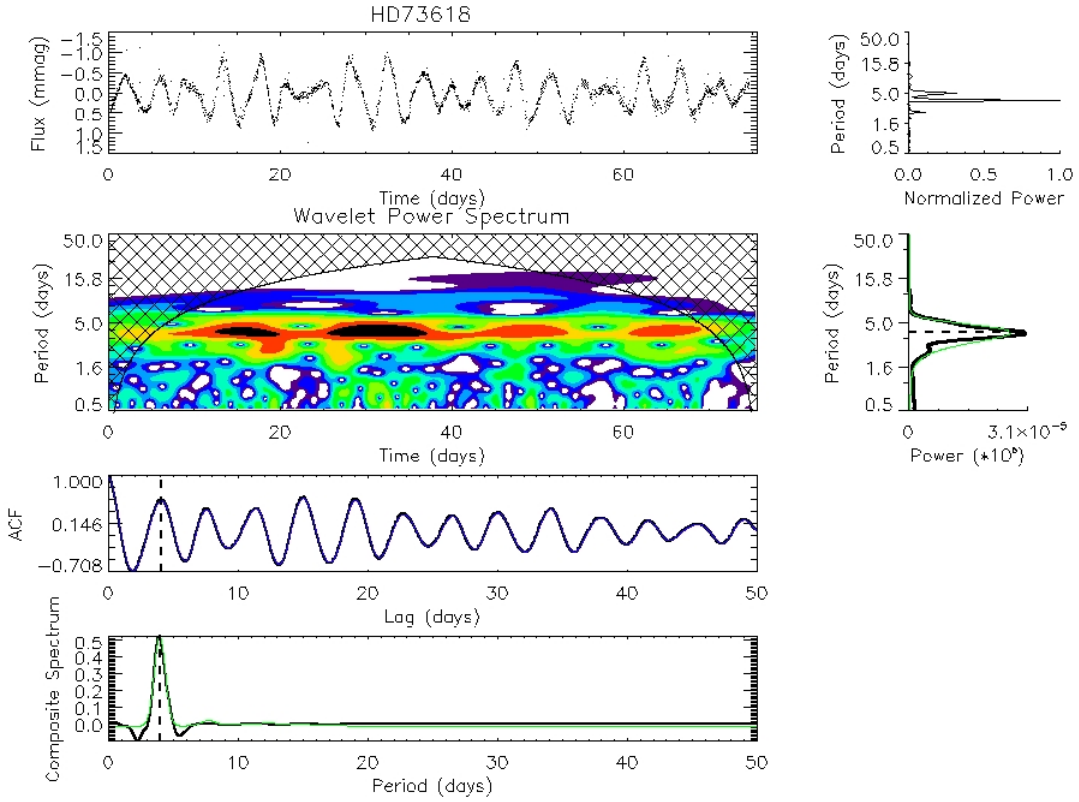

Figure B21. The wavelet map of HD 73618 based on *K2* C05 data. The description follows that for HD 73045, see Fig. 10.

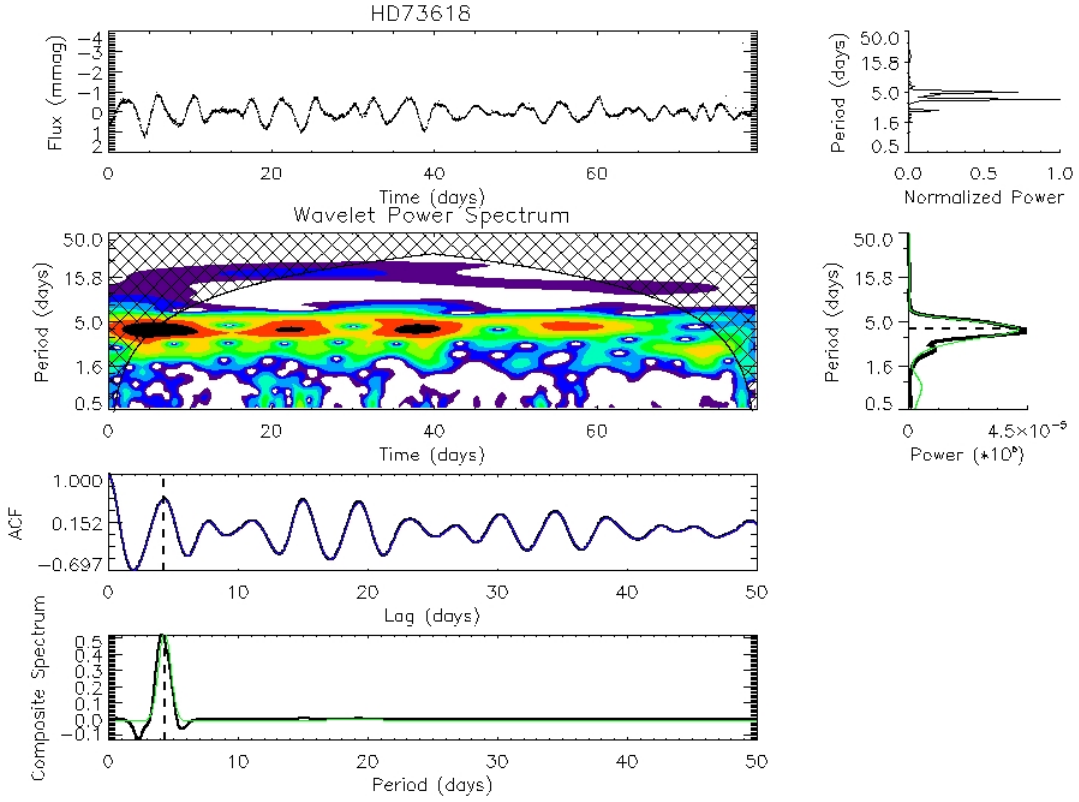

Figure B22. The wavelet map of HD 73618 based on *K2* C16 data. The description follows that for HD 73045, see Fig. 10.

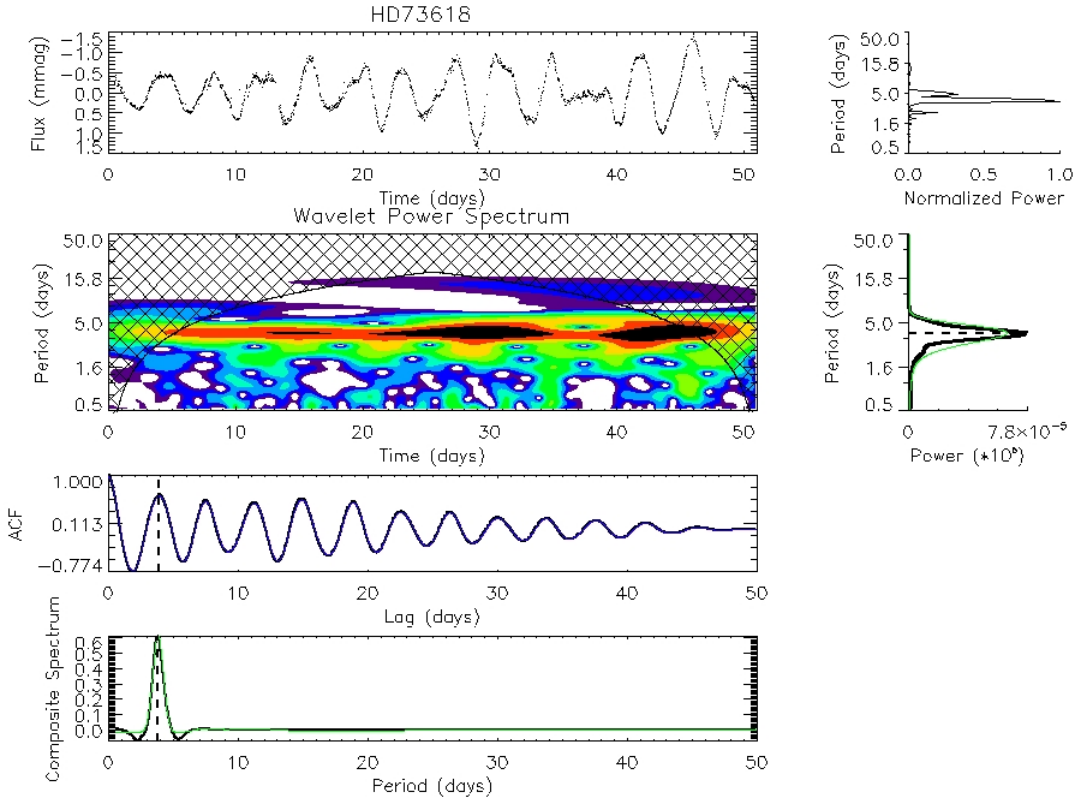

Figure B23. The wavelet map of HD 73618 based on C18 data. The description follows that for HD 73045, see Fig. 10.

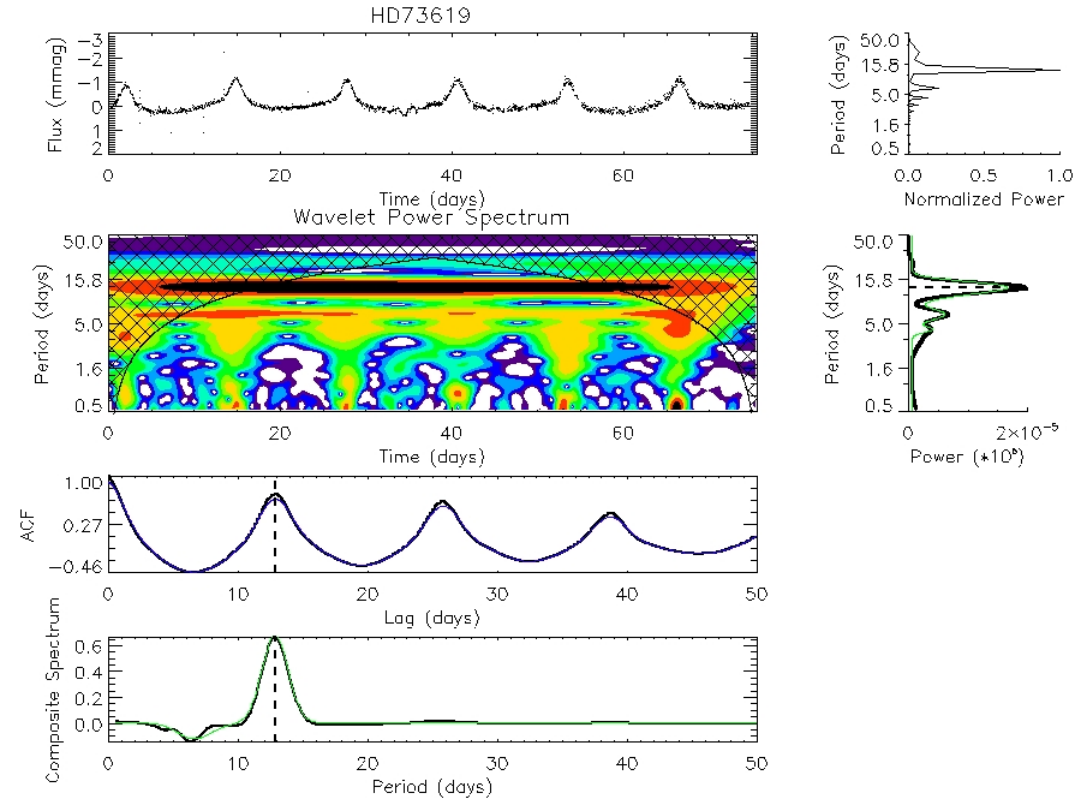

Figure B24. The wavelet map of HD 73619 based on *K2* C05 data. The description follows that for HD 73045, see Fig. 10.

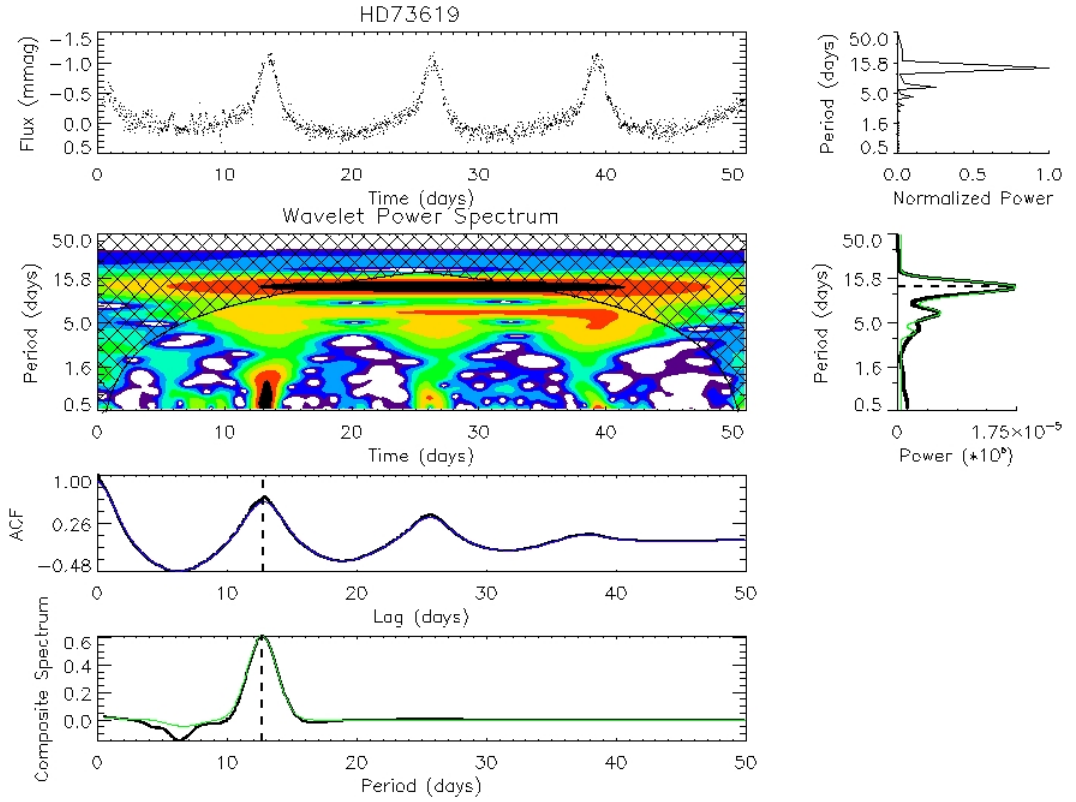

Figure B25. The wavelet map of HD 73619 based on C18 data. The description follows that for HD 73045, see Fig. 10.

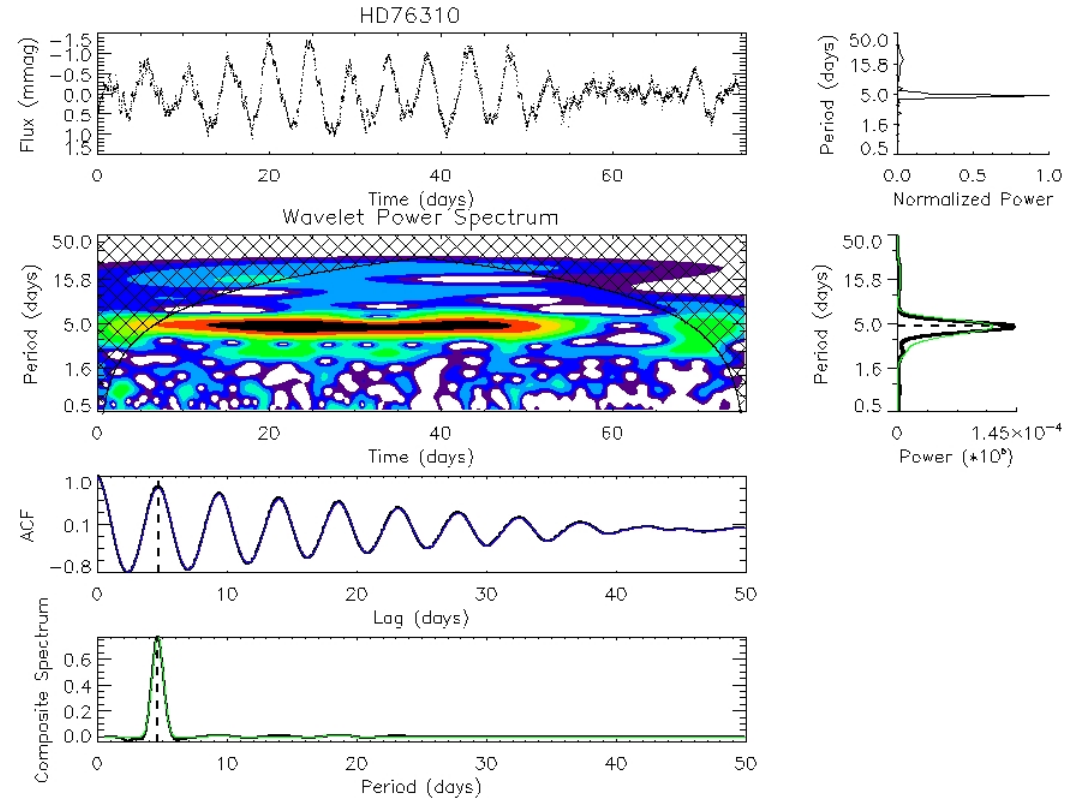

Figure B26. The wavelet map of HD 76310 based on C05 data. The description follows that for HD 73045, see Fig. 10.

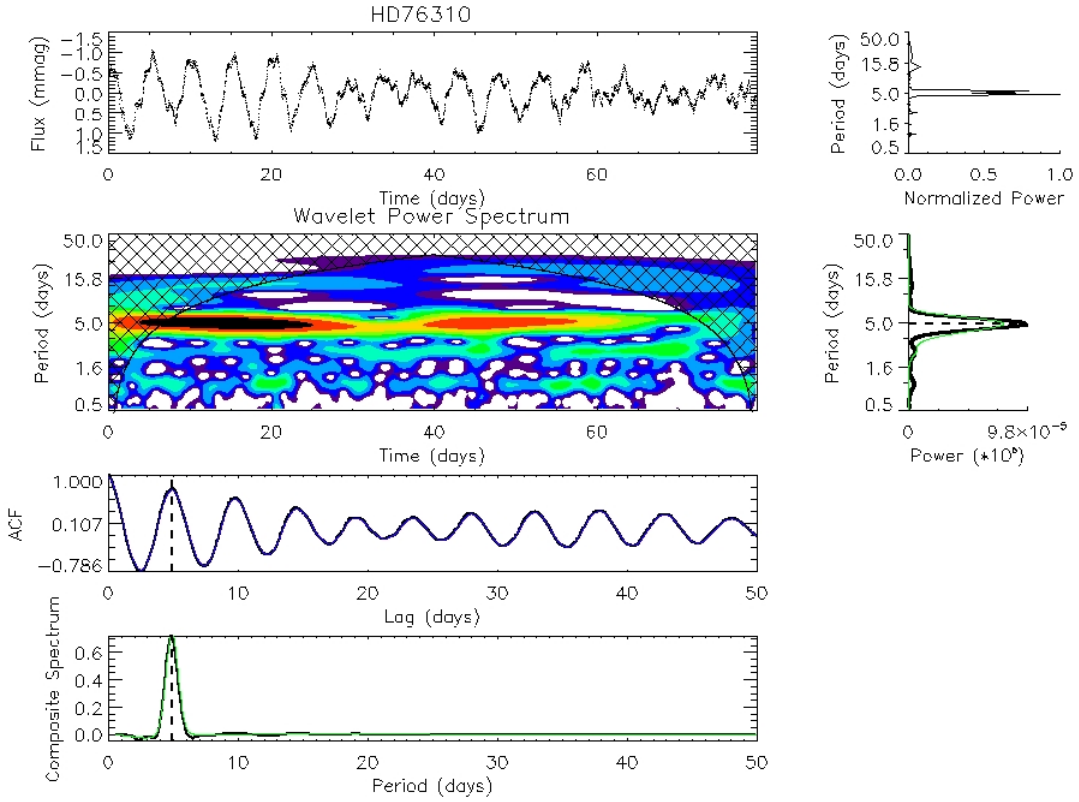

Figure B27. The wavelet map of HD 76310 based on *K2* C16 data. The description follows that for HD 73045, see Fig. 10.

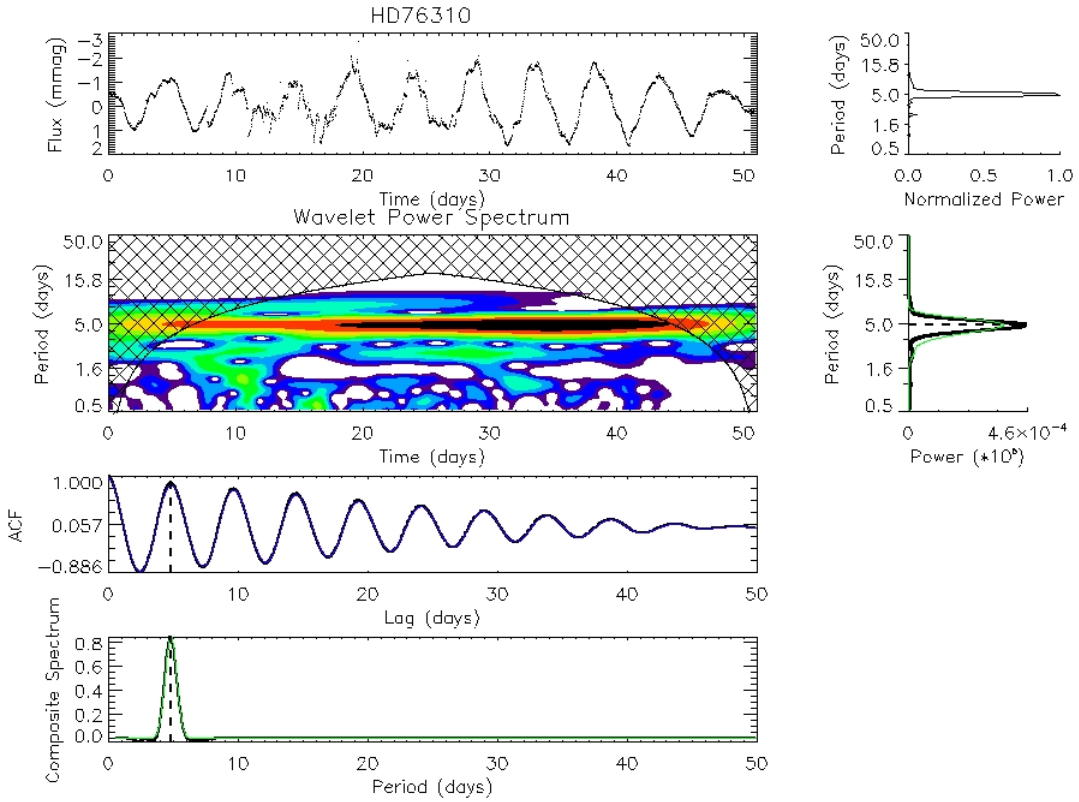

Figure B28. The wavelet map of HD 76310 based on *K2* C18 data. The description follows that for HD 73045, see Fig. 10.

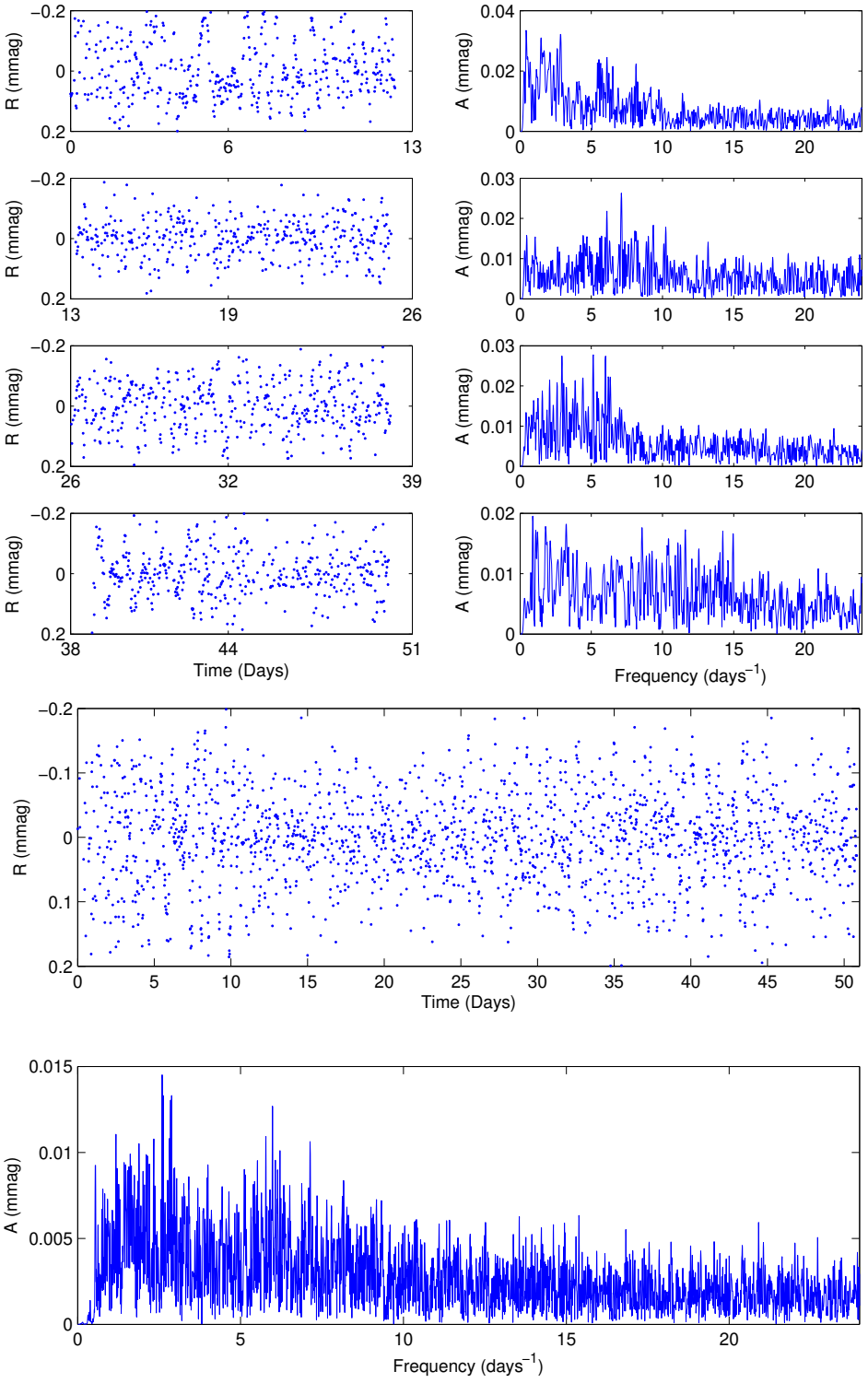

Figure B29. As Fig. 12, but for C18. Here the light curve was split into four segments. No evidence for pulsational signals is identified based on either method of analysis.

REFERENCES

Bowman D. M., Buysschaert B., Neiner C., Pápics P. I., Oksala M. E., Aerts C., 2018, A&A, 616, A77
Breger M., et al., 1993, A&A, 271, 482
Carquillat J.-M., Prieur J.-L., 2007, MNRAS, 380, 1064
Frescura F. A. M., Engelbrecht C. A., Frank B. S., 2008, MNRAS, 388, 1693
Lomb N. R., 1976, Ap&SS, 39, 447
Montgomery M. H., O'Donoghue D., 1999, Delta Scuti Star Newsletter, 13, 28
Scargle J. D., 1989, in Bulletin of the American Astronomical Society. p. 1069
VanderPlas J. T., 2018, ApJS, 236, 16

This paper has been typeset from a TEX/LATEX file prepared by the author.